In situ evidence of non-zero reflectance in the OLCI 1020 nm band for a turbid estuary

E. Knaeps [a,*], A.I. Dogliotti [b,c], D. Raymaekers [a], K. Ruddick [b], S. Sterckx [a]

[a] *Flemish Institute for Technological Research (VITO), Remote Sensing Unit (TAP), Boeretang 200, B-2400 Mol, Belgium*
[b] *Management Unit of the North Sea Mathematical Models (MUMM), Royal Belgian Institute for Natural Sciences (RBINS), 100 Gulledelle, B-1200 Brussels, Belgium*
[c] *Instituto de Astronomía y Física del Espacio (CONICET-UBA), Pab. IAFE, Ciudad. Universitaria, 1428 Buenos Aires, Argentina*

ARTICLE INFO

ABSTRACT

A spectroradiometer able to measure up to 2500 nm has been used to measure the reflectance for the Ocean and Land Color Instrument (OLCI) 1020 nm band. In July and October 2010 two measurement campaigns were organized at the Scheldt river to collect reflectance spectra and corresponding Total Suspended Matter (TSM) concentration and turbidity. A wide range of TSM concentration was covered from 15 to 402 mg L^{-1}. The measurements show a significant increase in reflectance between 950 and 1150 nm, corresponding to a decrease in the pure water absorption coefficient. A high correlation was observed between the reflectance at 1020 and 1071 nm and TSM concentration. The results were confirmed by simulations with Hydrolight and by the analysis of airborne Airborne Prism EXperiment (APEX) imagery.

© 2012 Elsevier Inc. All rights reserved.

1. Introduction

The Short Wave Infrared Region (SWIR, 1–3 μm) is characterized by strong water absorption with significant spectral variability. In remote sensing SWIR bands have been used to derive water content of vegetation, to estimate soil moisture and to identify and map minerals (*e.g.* Chen et al., 2005; Sgavetti et al., 2006). In ocean color however the SWIR has rarely been used. Based on the high absorption of pure water in this spectral region, the reflectance in the SWIR is generally assumed to be zero ("SWIR black pixel assumption") for clear and turbid waters (Gordon & Wang, 1994; Wang & Shi, 2007). For that reason, this spectral region was until 5–6 years ago not of interest for oceanographic research and the spectral coverage of pure ocean color sensors did not include the SWIR. For example, the Medium Resolution Imaging Spectrometer (MERIS) provides data up to 900 nm and the Sea-viewing Wide Field-of-view Sensor (SeaWiFS) up to 885 nm. Recently however it was shown that the SWIR signal provides vital information also for coastal and inland waters. Wang and Shi (2007) used the SWIR black pixel assumption to develop atmospheric correction schemes above water for the Moderate Resolution Imaging Spectroradiometer (MODIS). This atmospheric correction scheme was particularly important for turbid waters where reflectances are no longer zero in the Near InfraRed (NIR). Hence for these areas it provides an alternative to the NIR based atmospheric correction approaches developed by *e.g.* Moore et al. (1999), Lavender et al. (2005), Stumpf et al. (2003) and Ruddick et al. (2000). These investigators assumed a bright pixel in

the NIR and they all tried to remove the contribution of the water from the Top Of Atmosphere (TOA) NIR radiances, so that a "black pixel" could be provided to the standard atmospheric correction. The SWIR black pixel method has the advantage that it avoids the need for assumptions regarding near infrared optical properties used by the previous methods.

Despite the successful application of the SWIR atmospheric correction method for many turbid waters, the SWIR black pixel assumption seems to be no longer valid for extremely turbid waters. However, the Total Suspended Matter (TSM) concentration limit corresponding to 'extremely turbid' has not previously been documented and the only evidence against the SWIR black pixel assumption is image based. For instance, Shi and Wang (2009) assessed the SWIR black pixel assumption for the extremely turbid China east coastal and La Plata Estuary regions for the MODIS SWIR bands. The black pixel assumption was found to be generally valid with the MODIS SWIR bands at 1640 and 2130 nm even for extremely turbid waters. For the MODIS 1240 nm band, however, some slight radiance contributions were observed in extremely turbid waters. This implies that for these waters a modification is needed of the SWIR black pixel algorithm.

As a corollary of the need to modify atmospheric correction algorithms to account for a bright SWIR pixel, there is the opportunity to exploit this signal to retrieve information on the water constituents. As a logical extension of previous findings that near infrared wavelengths can be used for remote sensing of TSM in moderately turbid water (*e.g.* Doxaran et al., 2003; Nechad et al., 2010) the use of even higher, SWIR, wavelengths may be appropriate for remote sensing of even higher TSM concentrations.

The potential of using SWIR bands for atmospheric correction (Wang & Shi, 2007) has led to the inclusion of longer wavelength bands in new

* Corresponding author. Tel.: +32 14 336864; fax: +32 14 322795.
E-mail address: els.knaeps@vito.be (E. Knaeps).

ocean color instruments such as the Ocean and Land Color Instrument (OLCI) on Sentinel 3 to be launched in 2013. Moreover, there are a number of new airborne sensors, like APEX (Airborne Prism Experiment), and satellite instruments such as HyspIRI (Hyperspectral Infrared Imager), EnMAP (Environmental Mapping and Analysis Program) and VIIRS (Visible Infrared Imager Radiometer Suite), that will provide data in the SWIR in the near future. Further ocean color sensors with one or more SWIR bands are in various stages of design (*e.g.* the Argentine–Brazilian ocean color satellite SABIA/MAR mission and the Indian OCM-3ABC). A better understanding of SWIR reflectance will help in the design of these instruments and corresponding processing algorithms. As for the MODIS instrument, these wavelength bands provide new opportunities for atmospheric corrections in turbid waters and potentially for the retrieval of TSM concentrations in extremely turbid waters.

Despite these new opportunities to use the SWIR bands both for turbid water atmospheric correction and for the retrieval of TSM, there is a lack of field optical data in the SWIR to confirm assumptions on the SWIR reflectance. *In situ* reflectance measurements in the SWIR have not previously been reported to our knowledge. The main reason is photodetector hardware limitations. Only laboratory measurements in the SWIR performed by Chen et al. (1992) are reported, but these were too contaminated by noise in the SWIR and could not be used in further analysis.

In this paper *in situ* measured reflectance spectra in the SWIR will be presented for the first time for a highly turbid estuary and the spectral variability in the SWIR will be shown as function of TSM concentration and turbidity. The results from the *in situ* measurements are supplemented by numerical simulations with Hydrolight and hyperspectral APEX images.

The goal is to test the limits of the SWIR black pixel assumption for the OLCI band at 1020 nm for turbid water atmospheric correction and to indicate the potential of this spectral region for TSM retrieval. Our long term objective is to assess the impact of the non-zero reflectance in the SWIR on atmospheric correction, *i.e.* develop a bright pixel atmospheric correction in the SWIR. Finally, improvement of knowledge in the SWIR range would help optimize and standardize wavelengths for future sensors.

2. The OLCI 1020 nm band and pure water absorption

Before analyzing the *in situ* measured reflectance spectra, we take a closer look at the OLCI 1020 nm band and the pure water absorption spectrum. The pure water absorption coefficient as measured by Pope and Fry (1997) and Kou et al. (1993) is shown in Fig. 1 together with the central wavelength of the OLCI bands and the total atmospheric transmittance. The total atmospheric transmittance was simulated using the Modtran radiative transfer code for a platform height of 800 km (MERIS orbit height), a nadir view, a visibility of 17 km, a water vapor content of 2.5 m^{-1} and a rural aerosol.

The pure water absorption is low in the visible part of the spectrum and starts to increase around 600 nm. A first local maximum is observed at 755 nm. Then a more pronounced increase is observed leading to a second local maximum at 975 nm. After 975 nm there is again a decrease to reach a third absorption peak at 1196 nm. The atmospheric transmittance has lower values around the pure water absorption peaks.

The OLCI band at 1020 nm with 40 nm width is situated between the second and third absorption peak. Here absorption coefficients range between 19.8 and 40.7 m^{-1}. These locally lower absorption coefficients and high atmospheric transmittance indicate its potential for remote sensing.

3. Methodology

A flow chart of the methodology is presented in Fig. 2. The limits of the black pixel assumption will be assessed by 1) analyzing *in situ* above-reflectance spectra as function of TSM concentration and turbidity, 2) Hydrolight simulations and 3) the analysis of APEX airborne imagery. The corresponding field data needed for these analyses is shown in the flow chart. Additional coherence and quality checks for the field data are indicated with red arrows. The analysis of the *in situ* reflectance spectra is our prime focus as these are direct measurements of the SWIR reflectance. The Hydrolight simulations are used to confirm the results from these field data as they are independent of errors in the measurements methodology. Finally, APEX imagery is analyzed in the SWIR to check whether findings are affected by a low SNR (Signal to Noise Ratio) of the instrument or possible errors in the atmospheric correction. This last check is essential since SWIR spectral bands have in general lower SNR values than visible and NIR bands.

3.1. Study area

Our study area is part of the brackish lower sea Scheldt, situated between the city of Antwerp and the border of Belgium and the Netherlands. In this region there is a strong tidal influence. The tidal wave is semi-diurnal and propagates and extends up to Gent. The Scheldt is a relatively turbid estuary and TSM concentrations can reach maximum values up to 400 mg L^{-1} with strong tidal and seasonal variations (Arndt et al., 2007). Between the Dutch/Belgian border and the city of Antwerp there are large fluctuations in salinity ranging between 2 and 10 (Baeyens et al., 1998). All measurements were performed from a fixed pontoon (pontoon Sint Anna), located near the city of Antwerp (Fig. 3).
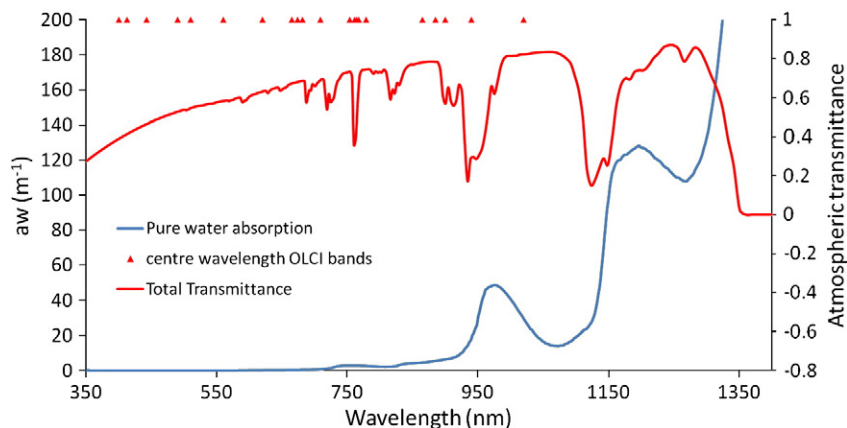

Fig. 1. Pure water absorption coefficient (Kou et al., 1993; Pope & Fry, 1997) and total atmospheric transmittance.
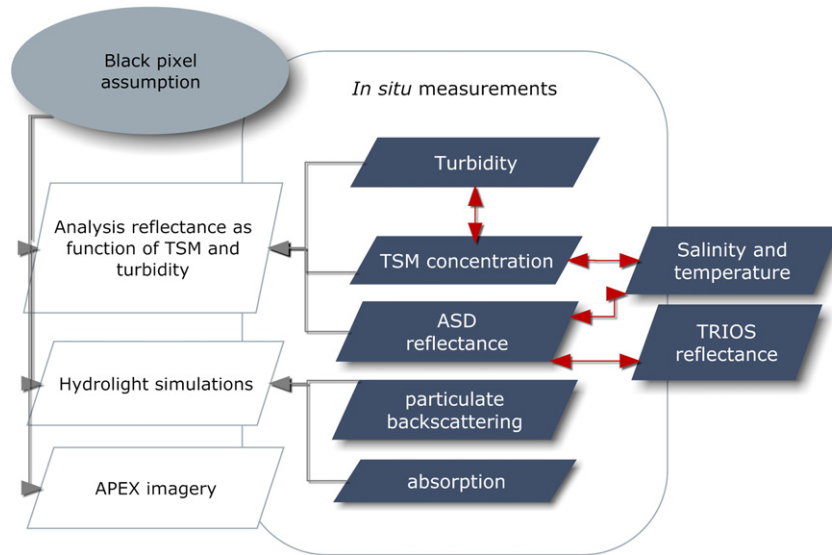
Fig. 2. Flow chart of the methodology.

3.2. Analysis of reflectance spectra

To test the black pixel assumption for the 1020 nm band reflectance spectra gathered in the field will be analyzed first. These reflectance measurements were collected at the Scheldt river using the ASD spectroradiometer. The measurements were performed from the Sint Anna pontoon on July 15 and on October 26 2010, starting around 10:00 local time ending around 15:00 local time. On both days the sky was generally (not fully) overcast.

To analyze these data as function of TSM concentration and turbidity, extra *in situ* data was collected coincidently with the ASD measurements. Water samples were collected to retrieve the TSM concentration and turbidity. For coherence and quality checks, extra reflectance measurements were made with TriOS spectroradiometers and a CTD (Conductivity–Temperature–Depth) probe was used to record salinity and temperature. The TriOS reflectance data will be used to check the ASD measurement methodology in the VNIR and a time series of salinity, temperature, TSM and reflectance
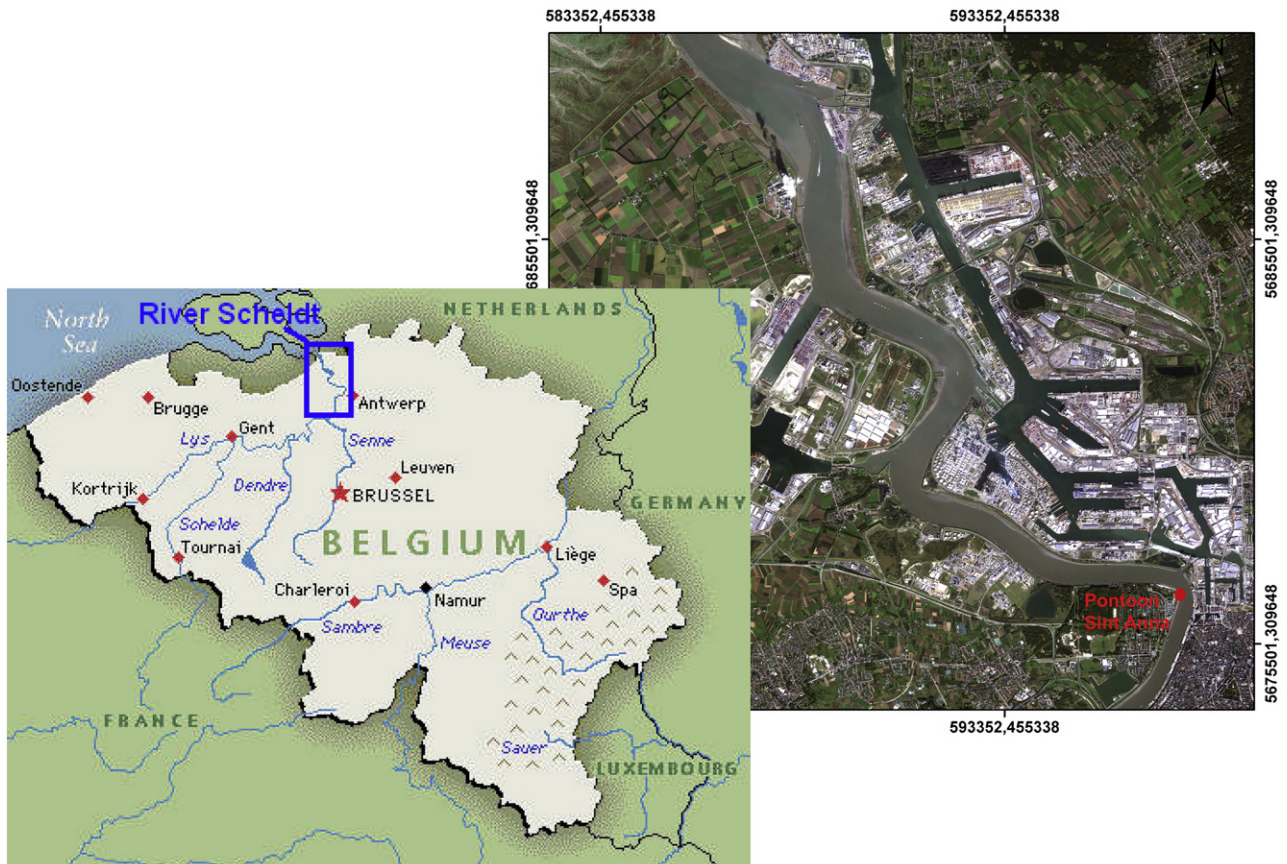

Fig. 3. Scheldt study site and location of pontoon Sint Anna near Antwerp.

can be used to check the coherence of all the optically related parameters.

Finally the reflectance spectra were resampled to the OLCI spectral bands to check the influence of the OLCI spectral band width on the results. The OLCI 1020 nm band has a corresponding spectral width of 40 nm compared to a spectral width of 10–12 nm for the ASD measurements in the SWIR.

3.2.1. TSM concentration

From the water samples TSM concentration was determined by filtering the water on Whatman GF/F glass fiber filters according to the European reference method EN 872 (2005). Following this method, the dry weight of the filters without particles is first measured. Next the filters are moistened with MilliQ-water. After shaking, 250 mL of the water samples is filtered. Then the filter is rinsed 3 times with 150 mL MilliQ-water to wash out the salt. The filter is dried in the oven for minimum 2 h at 105 °C and is subsequently cooled in a desiccator for minimum half an hour. Finally, the filter is weighted and the concentration is derived.

3.2.2. Turbidity

Turbidity was measured with a portable HACH 2100P ISO turbidimeter as in Nechad et al. (2009). The instrument records turbidity between 0 and 1000 Formazin Nephelometric Units (FNU), with a resolution of 0.01 FNU. The average response over 10 measurements at 1.2 s intervals is taken (signal averaging) and the auto-range function is used. Turbidity was measured on the water samples within 30 min of sampling. Three replicate turbidity measurements were recorded for each water sample, gently tumbling the sample cell three times between each turbidity measurement. The mean value was used here. The turbidimeter was first calibrated in April 2007 using a set of Stabilized Formazin Turbidity Standards (STABLCAL) with turbidities of <0.1, 20, 100 and 800 FNU, prepared according to the instructions of the manufacturer. Turbidities of these standards were also recorded after each sampling day in July and October to check the instrument stability.

3.2.3. Reflectance

The reflectance was measured with an ASD FieldSpec FR spectrometer. The ASD spectrometer measures the backscattered light from the water body and the light reflected at the air–water interface in the Visible/Near Infrared (VNIR, 350–1050 nm) and the Short-Wave Infrared (SWIR, 900–2500 nm) part of the spectrum. The VNIR spectrometer has a spectral resolution of approximately 3 nm at around 700 nm. The spectral resolution in the SWIR varies between 10 nm and 12 nm. The downwelling irradiance above the surface ($E_d(0+)$) was measured using an almost 100% reflecting Spectralon reference panel (Analytical Spectral Devices, Inc.). Then, the total upwelling radiance from the water ($L_u(a)$) (i.e. from the water and from the air–sea interface) was measured by pointing the sensor at the water surface at 40° from nadir, maintaining an azimuth of 90° or 135° from the solar plane, depending on the pontoon orientation with respect to the sun. Downwelling sky radiance ($L_{sky}(a)$) was measured at a zenith angle of 40° to account for the skylight reflection. In July these measurements were performed with one ASD, thereby measuring E_d, L_u and L_{sky} successively. In October two ASD instruments were used; one ASD measuring the sky radiance continuously, the second ASD measuring $E_d(0+)$ and $L_u(a)$ alternately. The second measurement set-up allows to minimize the sampling time between the three individual measurements.

The reflectance (R_w) was calculated using the following equation (Mobley, 1999):

$$R_w = \pi \left(L_u(a) - \rho_{as} L_{sky}(a) \right) / E_d(0+) \qquad (1)$$

where ρ_{as} is the air–sea interface reflection coefficient. This is set to a fixed value of 0.0256 for the Scheldt instead of the wind speed formula of Ruddick et al. (2006), because surface gravity waves are not expected to be as strongly wind speed dependent in a narrow estuary. An extra correction was performed for residual sky glint by subtracting the reflectance remaining at 1200 nm, supposing that sky glint is relatively white in spectral shape under cloudy conditions (Toole et al., 2000).

In addition, a comparison between the TriOS and ASD reflectances measurements is made to quality control the ASD methodology for the VNIR spectral range covered by both instruments. The two instruments were installed at the pontoon a few meters apart. Three TriOS-RAMSES hyperspectral spectroradiometers, two measuring radiance and one measuring downwelling irradiance were mounted on a steel frame (Hooker & Lazin, 2000); zenith angles of the sea- and sky-viewing radiance sensors were 40°. Two different deployments were set; in July the frame was fixed at the edge of the pontoon, while in October a special device was constructed so the frame could be deployed away from the pontoon. In both cases the frame was rotated to achieve the 135° or 90° relative azimuth angle for viewing. The sensors measured over the wavelength range 350–900 nm with sampling interval of approximately 3.3 nm and spectral width of about 10 nm. Data were acquired with the MSDA software and radiometrically calibrated using nominal calibration constants. Calibrated data for $E_d(0+)$, $L_u(a)$, and $L_{sky}(a)$ were interpolated to 2.5 nm intervals and then corrected to the latest calibration of the sensors (July 2010). The measurements used were the average of five acceptable scans around the time of ASD acquisition (details of the processing and quality control are described in Web Appendix 1 of Ruddick et al., 2006).

3.3. Hydrolight simulations

Having tested the limits of the black pixel assumption with field data, simulations of reflectance in the VNIR-SWIR were performed with Hydrolight to confirm the results. To extend Hydrolight beyond 1000 nm the pure water absorption measured by Pope and Fry (1997) and Kou et al. (1993) (Fig. 1) was used and sky irradiance beyond 1000 nm was generated with MODTRAN. The simulations were performed using the mean optical properties measured at the Scheldt river (Sections 3.3.1 and 3.3.2), $a_{CDOM}(440)$ of 1.1 m^{-1}, a Chlorophyll concentration of 30 μg/L^{-1} and TSM concentrations varying between 10 and 300 mg L^{-1}.

3.3.1. Backscattering measurements

On October 26, 2010, an ECO-BB3 from Wetlabs measuring volume scattering was attached to the pontoon and logged continuously starting from 10:23 to 15:10 local time. The ECO-BB3 meter records information at three wavelengths: 440 nm, 595 nm and 780 nm. The raw data was converted into particulate backscattering coefficients, $b_{bp}(\lambda)$ according to the Wetlabs user's guide (Wetlabs, 2008). The specific backscatter was derived by relating the backscatter to the measured TSM concentration for 14 measurements. For their further use in the simulation of reflectance, a power-curve was fitted through these points. The fitting of such a power-law curve is supported by recent studies (e.g. Snyder et al., 2008) that suggest that particulate backscatter spectra are generally smooth and follow a power law distribution except where particulate absorption effects are strong, e.g. near 665 nm for phytoplankton (Bricaud & Morel, 1986). Mie theory applied to infinite Junge-type particle size distributions (Morel & Prieur, 1977) suggests that such a power law distribution will continue in the SWIR with a similar spectral exponent. It is recognized that a power law might not always be representative, but in the absence of backscatter measurements in the SWIR, this extrapolation is needed to attain information at the longer wavelengths. The average backscattering coefficient and standard deviations are presented in Fig. 4.
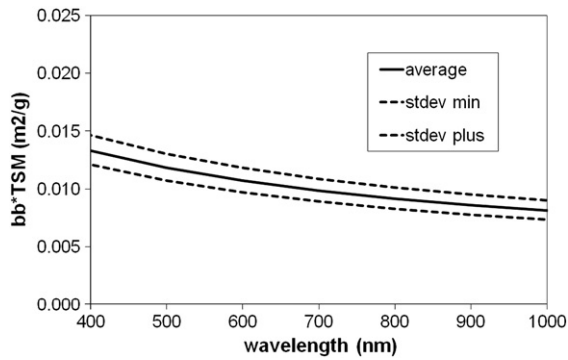
Fig. 4. Specific particle backscattering coefficients from October 2010, measured at pontoon Sint Anna.

3.3.2. Total absorption

In 2009 the absorption of colored dissolved organic matter (CDOM) (a_{CDOM}), Chlorophyll (a_{chl}) and Non-Algae Particles (a_{nap}) was measured from water samples collected at the pontoon in the Scheldt river. The specific absorption spectra of non-algae particles and Chlorophyll were measured using the filter pad method using a LICOR integrating sphere attached to an ASD spectrometer following the methods described by Tassan and Ferrari (1995) and REVAMP (Regional validation of MERIS chlorophyll products in North Sea coastal waters) protocols (Tilstone et al., 2003).

For the CDOM absorption, the water samples from the field campaign were temporarily stored in a cooled chamber and filtered through 0.2 μm pore size filters. To retrieve the CDOM absorption coefficient of the water samples, the beam attenuation of the filtered water was measured with Ocean Optics equipment in a transparent cuvet. As the data from the ocean optics equipment are noisy for wavelengths <400 nm and >950 nm the exponential shape of the CDOM absorption (a_{CDOM}) was fitted based on the 420–750 nm wavelength range.

3.4. APEX image analysis

On 23th June 2010, hyperspectral airborne data were acquired from the Scheldt river near Antwerp city with the APEX (Airborne Prism Experiment) sensor on board of a Dornier Do228 (Fig. 5). APEX is developed by a Swiss–Belgian consortium on behalf of ESA. It is intended as a simulation, calibration and validation device for spaceborne imagers. APEX records hyperspectral data in approximately 300 bands in the wavelength range between 380 and 2500 nm (Itten et al., 2008). The APEX

radiometric, spectral, and geometric calibration is performed by means of the Calibration Home Base (CHB) hosted at DLR Oberpfaffenhofen, Germany (Gege et al., 2009). The atmospheric and air-interface correction of the acquired APEX data is performed with the MODTRAN-5 radiative transfer code following the algorithms given in de Haan et al. (1991) and de Haan and Kokke (1996). Details on the algorithms and implementation are given in Sterckx et al. (2011). Residual sky glint is corrected for by subtracting the reflectance remaining at 1203 nm. Finally, a mild spectral smoothing of the data is performed to remove noise and spikes remaining after atmospheric correction due to systematic gain and offset errors. This is performed with the EFFORT software (Boardman, 1998) in ENVI (Boulder, CO: ITT Visual Information Solutions) EFFORT uses the data to generate "pseudo field" spectra by fitting each observed spectrum with a parametric model of Legendre polynomials. Gains and offsets for every band are calculated by comparing the modeled spectra to the data spectra, for pixels that are well-fit. The aerosol optical depth and Ångström exponent are obtained from ground-based sunphotometer readings performed with a MICROTOPS sunphotometer during the overpass of the airplane.

4. Results

4.1. Reflectance as function of TSM and turbidity

4.1.1. TSM and turbidity data

In July large variations in TSM concentration and turbidity were recorded. TSM concentration ranged from 15 to 402 mg L^{-1} and turbidity from 53.7 to 282.7 FNU. In October variations were smaller. TSM concentration ranged from 55 to 130 mg L^{-1} and turbidity ranged from 52.3 to 101 FNU. The relationship between TSM concentration and turbidity is shown in Fig. 6. In this figure two outliers can be observed in red (superimposed) which will be excluded from further analysis. It is not clear what may have caused these outliers, but based on the relationship between tidal cycle and sampling time (Section 4.1.4) it is expected to have higher concentrations than those retrieved from the TSM analysis. After removal of these two outliers the correlation coefficient is 0.99, the slope is 0.7 and the intercept 15.11.

4.1.2. Quality check in the VNIR using TriOS data

Fig. 7 shows some reflectance spectra in the VNIR measured with the ASD and TriOS and Fig. 8 shows the correlation between both instruments for some discrete wavelengths. Overall the spectra match very well. For the spectra shown in Fig. 7 the root mean square error (RMSE) for all wavelengths is 0.006. The correlation for the discrete
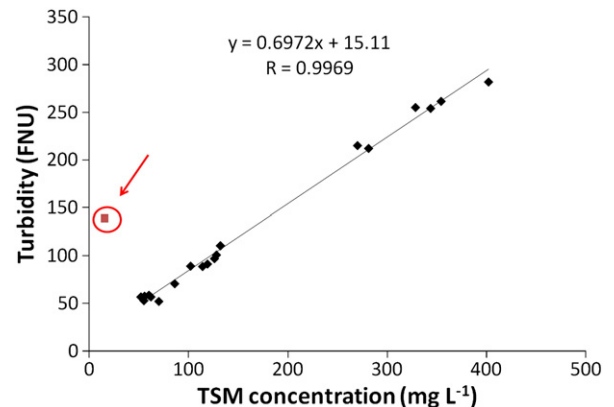

Fig. 5. APEX instrument installed in Dornier Do228 aircraft.

Fig. 6. Relationship between TSM concentration and turbidity.
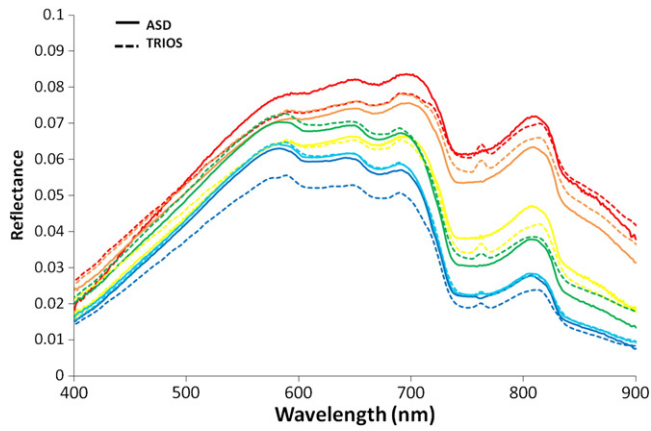
Fig. 7. Intercomparison of ASD and TriOS reflectance measurements; complete spectra.

wavelengths presented in Fig. 8 is 0.99. Small differences in reflectance are thought to arise mainly from the in-water spatial variation in optical constituents between the two measurement locations. In general, based on these results, it can be concluded that the measurement methodology for the ASD seems correct.

4.1.3. VNIR-SWIR spectra as function of TSM and turbidity

The ASD reflectance in the VNIR and SWIR measured on both days is shown in Fig. 9. The corresponding TSM concentrations are shown, with black and red colors indicating the highest TSM concentrations and blue colors the lowest concentrations. Overall the measurements of July have a higher reflectance than those from October, reflecting the differences in TSM concentrations. The spectra from October exhibit more noise, particularly in the oxygen absorption band (~762 nm), which can be attributed to very small shifts in the wavelengths between the two ASD instruments. As found in previous studies, e.g. Doxaran et al. (2003), reflectance for the blue-green region is seen to be only weakly sensitive to variation of TSM in the high concentration range with a 7–8 fold increase in TSM giving only ~50% increase in reflectance at 550 nm. For such spectra the reflectance is approaching an asymptotic or natural "saturation" threshold (Bowers et al., 1998). Between 550 and 950 nm a change in shape and magnitude is observed in the spectra with increasing TSM concentration. For the lowest TSM concentrations a maximum is observed around 580 nm. With increasing TSM concentrations

the signal between 580 nm and 680 nm changes in shape and the peak is now observed around 680 nm. Toward longer wavelengths the signal in the NIR is weakening to reach a minimum around 950 nm. In the OLCI band region around 1020 nm the reflectance is clearly not zero. A significant increase in reflectance can be observed for both days between 950 and 1150 nm with a peak around 1071 nm. This spectral region completely matches with the decrease in the pure water absorption spectrum (Fig. 1).

For both days, the spectra of more turbid water seem to have a larger contribution between 950 and 1150 nm. This is confirmed by plotting the reflectance at 1020 nm against TSM (Fig. 10a) and turbidity (Fig. 10b). For comparison also the reflectance at 1071 nm is plotted against TSM (Fig. 10c) and turbidity (Fig. 10d). This spectral band is situated in the center of the SWIR reflectance increase between 950 and 1120 nm. A strong correlation is observed for the 1020 nm band with a correlation coefficient of 0.82 for TSM and 0.88 for turbidity. For the 1071 nm band, located in the SWIR reflectance peak, a correlation coefficient is found of 0.96 and 0.95 for TSM and turbidity respectively. Hence these results reject the black pixel assumption and they also reveal the possibilities of the SWIR to derive TSM concentration for highly turbid waters. For the spectral band at 1071 nm the correlation was stronger than for the OLCI 1020 nm band.

Additionally the regression equations of all four plots are shown in Fig. 10. From these equations it is possible to quantify the limits of the black pixel assumption at 1020 and 1071 nm in terms of TSM concentration and turbidity by applying a certain threshold reflectance. For a threshold reflectance of 0.002 at 1020 nm, a limit of 35 mg L^{-1} for the TSM concentration and 46.7 FNU for the turbidity can be derived. For the same threshold at 1071 nm, a limit of 17.5 mg L^{-1} for the TSM concentration and 23.3 FNU for the turbidity is found. Hence for higher concentrations, corresponding to extremely turbid waters, a bright pixel algorithm will be needed for atmospheric correction using these bands.

To investigate the effect of the non-zero reflectance for the OLCI 1020 nm band, the reflectance spectra from July were resampled to the OLCI bands (Fig. 11). Although the OLCI 1020 nm band has a spectral width of 40 nm, there is still a significant increase in reflectance observed with increasing TSM concentrations, as in Fig. 9.

4.1.4. Coherence check with temperature and salinity

Additionally, two time series are presented in Figs. 12 and 13 for measurements performed in July at pontoon Sint Anna. In time series 1 (Fig. 12) the decrease of the TSM concentrations and the reflectance
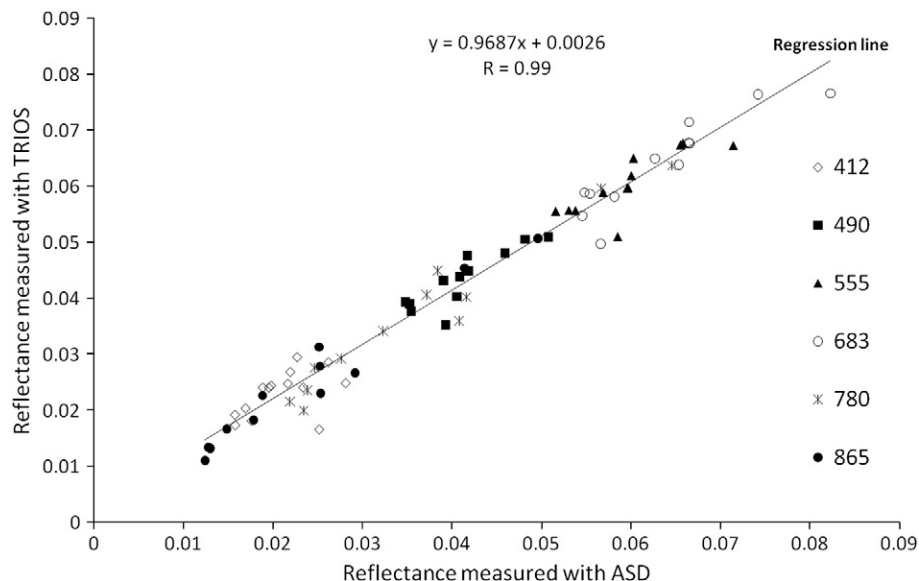

Fig. 8. Intercomparison of ASD and TriOS reflectance measurements; discrete wavelengths.
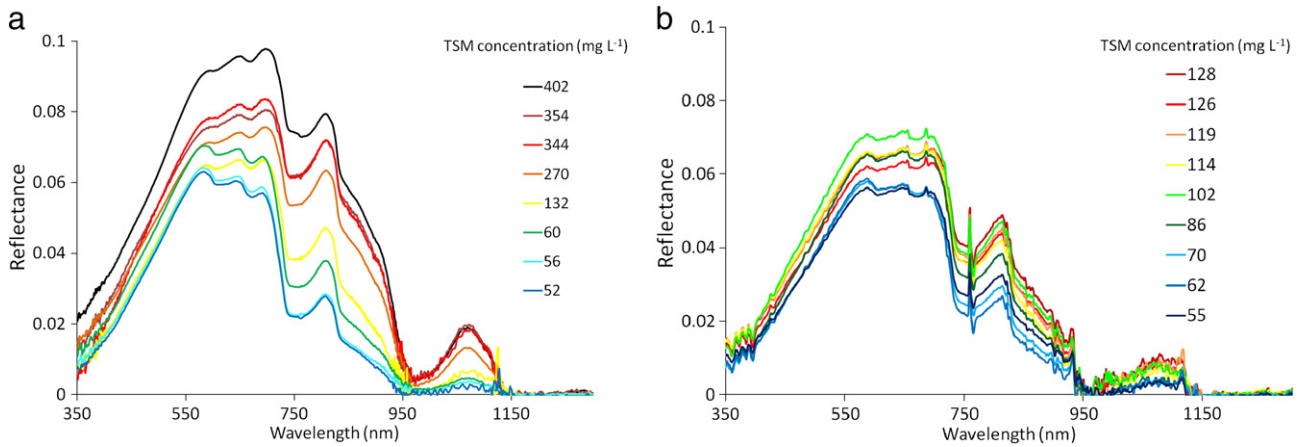
Fig. 9. Reflectance measured in a) July and b) October. Corresponding TSM concentrations are indicated in mg L^{-1}.

at 870 nm, 1020 nm and 1071 nm over the tidal cycle is presented. The measurements started at 9:36 local time and end at 15:36 local time. Time series 2 (Fig. 13) shows the increase in temperature and decrease in salinity over the same time period.

On the measurement day there was High Water (HW) around 7:00 local time and Low Water (LW) around 14:04 local time. At the onset of the ebb flow stage, ~45 min. after HW, there is a movement of freshwater into the estuary. A resuspension of sediment

takes place, especially at the bend-related shoals (e.g. location Sint Anna pontoon). During ebb TSM concentrations gradually decrease. At the same time we observe a decrease in salinity and an increase in temperature. These two parameters give an indication of the sea-water intrusion (river water warmer than seawater in summer). Around LW, low TSM concentrations are observed because of low cur-rent velocities and hence lower resuspension. At the onset of the flood flow stage there is a movement of marine water into the estuary
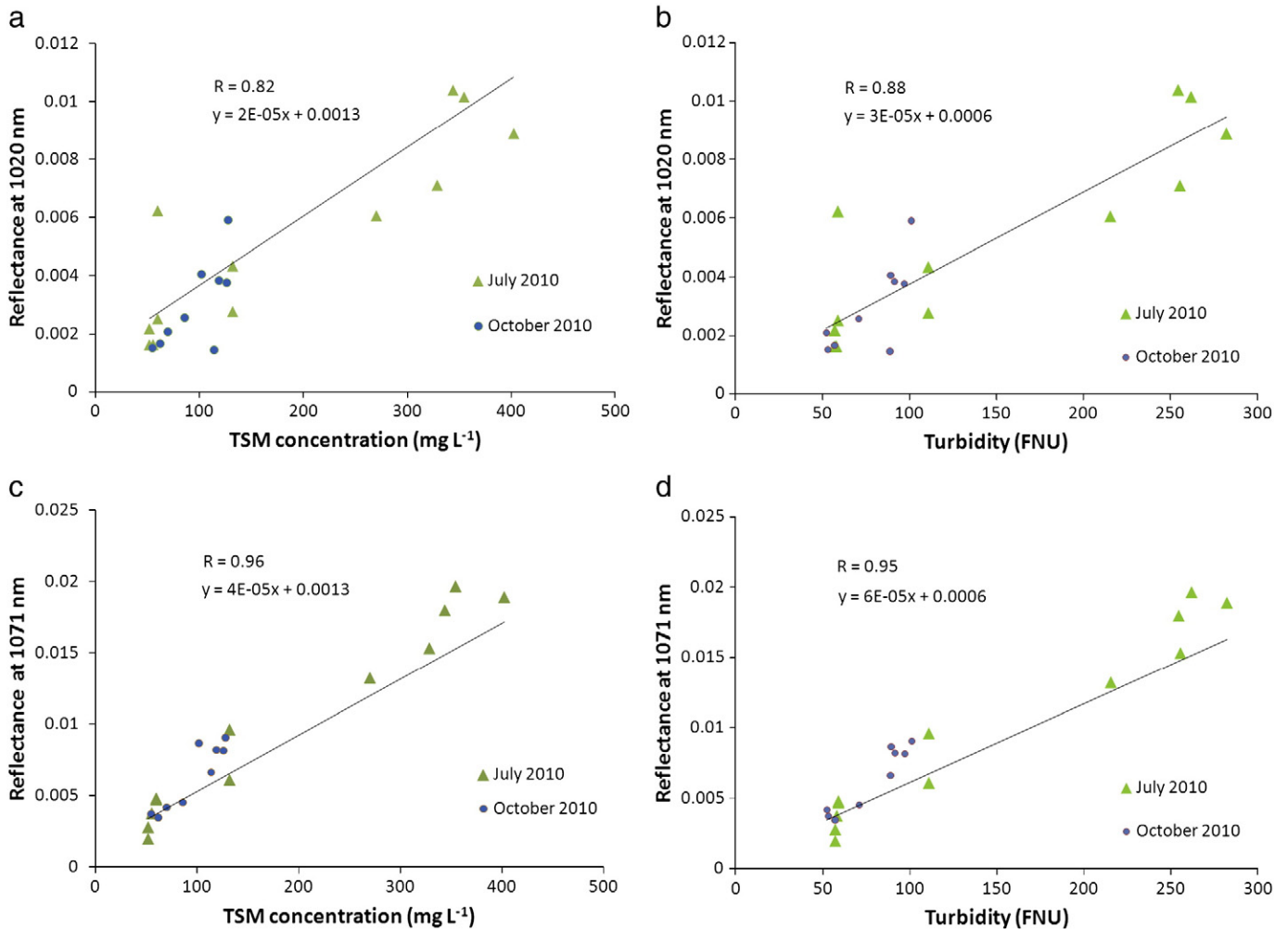

Fig. 10. Correlations between TSM and a) reflectance at 1020 and c) reflectance at 1071; Correlations between turbidity and b) reflectance at 1020 and d) reflectance at 1071.
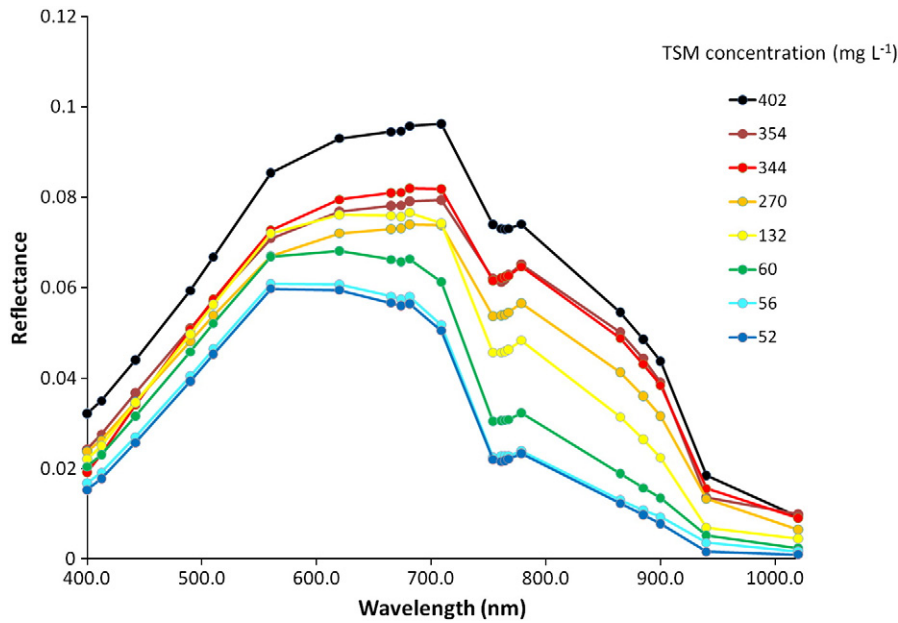
Fig. 11. Reflectance spectra measured in July resampled to the OLCI bands.

leading to an increase in salinity and again a resuspension of sediment by tidal movement (Fettweis et al., 1998).

The reflectance in the NIR and SWIR follow these changes in the tidal cycle. Hence these Figures show the large variability present in all parameters and show the coherency for all optically-related parameters.

4.2. Hydrolight simulations

The results from the Hydrolight simulations are shown in Fig. 14. In the VNIR spectral region there is a gradual increase in reflectance with increasing TSM concentration. The change in spectral shape between 580 and 680 with increase in TSM is less pronounced than the change observed in Fig. 9 for the *in situ* measurements. Differences in reflectance between the Hydrolight simulations and the *in situ* measurements can be attributed to changes in optical properties between the sampling dates. These changes in optical properties can be the result of changes in sediment composition during the seasons. Nevertheless the Hydrolight simulations show non-zero reflectance in the 950–1150 nm region. Furthermore the reflectance increases with

TSM concentration. These results again reject the black pixel assumption around the OLCI 1020 nm band for the Scheldt river. They provide an independent check of the ASD measurement results not influenced by any instrument noise or methodological errors.

4.3. APEX image analysis

The RGB combination of the APEX image acquired over the Scheldt river on 23th June 2010 is shown in Fig. 15a. Fig. 15b shows the ratio of the reflectance at 711 nm and at 597 nm. This ratio has shown to be exponentially related to the TSM concentration in the Scheldt river (Knaeps et al., 2010). Fig. 15c and d shows a map of the reflectance at 1069 nm, located near the SWIR reflectance peak, and 1020 nm, corresponding to the OLCI band, respectively. Patterns in high turbid zones are very similar in the different figures indicating a clear relationship between TSM and the reflectance at 1020 or at 1069 nm. Highest values are observed near the Sint Anna pontoon which is known to be situated at the turbidity maximum of the Scheldt river. TSM concentration up to $292 \, mg \, L^{-1}$ was measured at Sint-Anna during the flight. Lower values are observed downstream, especially
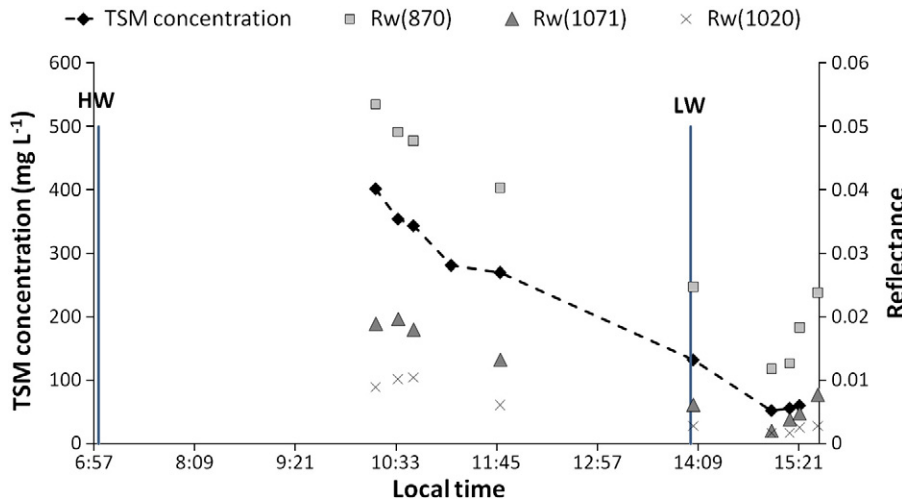

Fig. 12. Time series of TSM concentration, Rw(870), Rw(1020) and Rw(1071) measured in July.
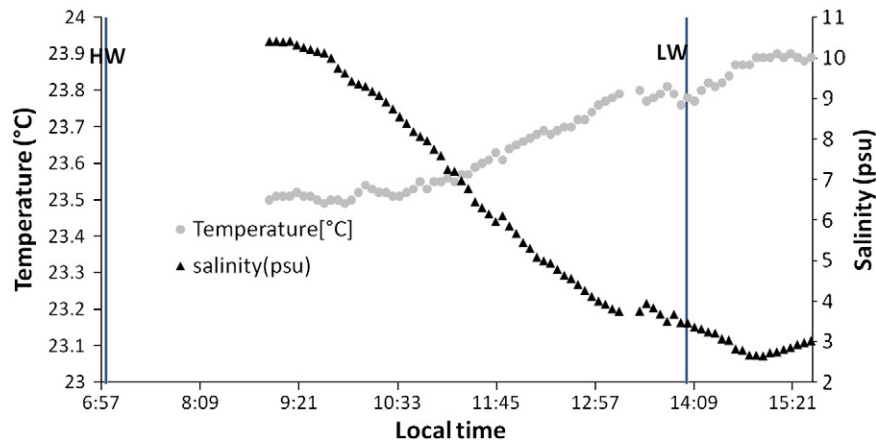
Fig. 13. Time series of temperature and salinity measured in July.

in the fairway. For the lower turbidity zones (blue colored areas in Fig. 15) the noise of the APEX sensor is clearly limiting the detection level more at 1020 nm than at the 1069 nm near the SWIR reflectance peak. SWIR readout noise (i.e. electrons introduced into the final signal upon the readout of the device) artifacts are visible as vertical stripes every 250 pixels. This is caused by the fact that the SWIR detector of APEX is read out in 4 groups of 250 pixels. The two vertical lines are caused by two thin wires glued on the instrument slit for assessment of the geometric stability of the system. With a minimum radiance at 1050 nm of 4 $mWm^{-2}nm^{-1}sr^{-1}$ and a Noise Equivalent Delta Radiance (NeDL) around 0.14 $mWm^{-2}nm^{-1}sr^{-1}$, the APEX SWIR detector is however not designed for water quality monitoring. It is expected that the noise in the 1020 nm band of the OLCI sensor, which has a lower minimum radiance limit (i.e. 1.81 $mWm^{-2}nm^{-1}sr^{-1}$) and a better SNR at low radiances, will be a less limiting factor than in the case of APEX.

In Fig. 16 APEX reflectance spectra (omitting the water vapor absorption regions between 900 and 1000 nm) are given for the eight locations indicated in Fig. 15. Again little variability is seen in the blue-green wavelengths, with most differences found in the near infrared and SWIR. A local reflectance peak is observed around 580 nm for the spectra with lowest TSM concentrations. The red spectra, corresponding to higher TSM concentrations, are much flatter between 580 and 680 nm. The same change in spectral shape was observed for the in situ measurements. Similar to the results from the in situ measurements and Hydrolight simulations a local reflectance maximum is observed in the SWIR at 1070 nm.

5. Discussion and conclusion

In this paper the limits of the black pixel assumption have been assessed for the Scheldt river based on in situ reflectance spectra, supported with Hydrolight radiative transfer simulations and the analysis of APEX imagery. Based on the reflectance spectra measured in the field, a significant increase in reflectance was observed between 950 and 1150 nm where pure water absorption has a local minimum. A reflectance peak was observed around 1071 nm. The Hydrolight numerical simulations confirmed the non-zero reflectance in this spectral region and provided an independent check not influenced by any instrument noise or methodological errors. Moreover, SNR and atmospheric influences does not seem to alter these findings as similar increases were found in the APEX imagery. Of course for other type of sensors this analysis has to be performed again as the SNR is specifically linked to the instrument. Several quality and consistency checks between two different reflectance measurement systems and between various optical parameters give confidence in the measurement methodology.

These findings can be seen as a trivial extension of previous findings for the near infrared spectral range (Ruddick et al., 2006), except that for the SWIR range the pure water absorption is much higher and, hence, effects become detectable only for relatively high TSM concentrations.

Further, a TSM concentration limit for application of the black pixel assumption could be specified using a reflectance uncertainty of 0.002. It can be concluded that for this 0.002 reflectance threshold
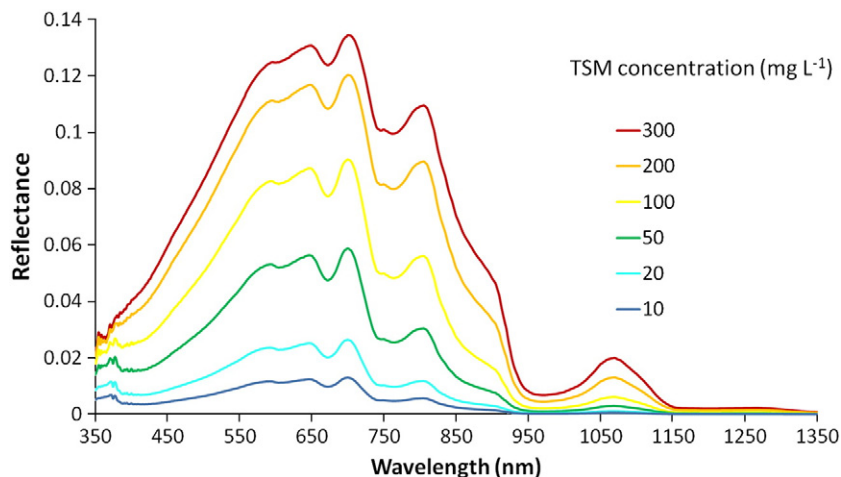

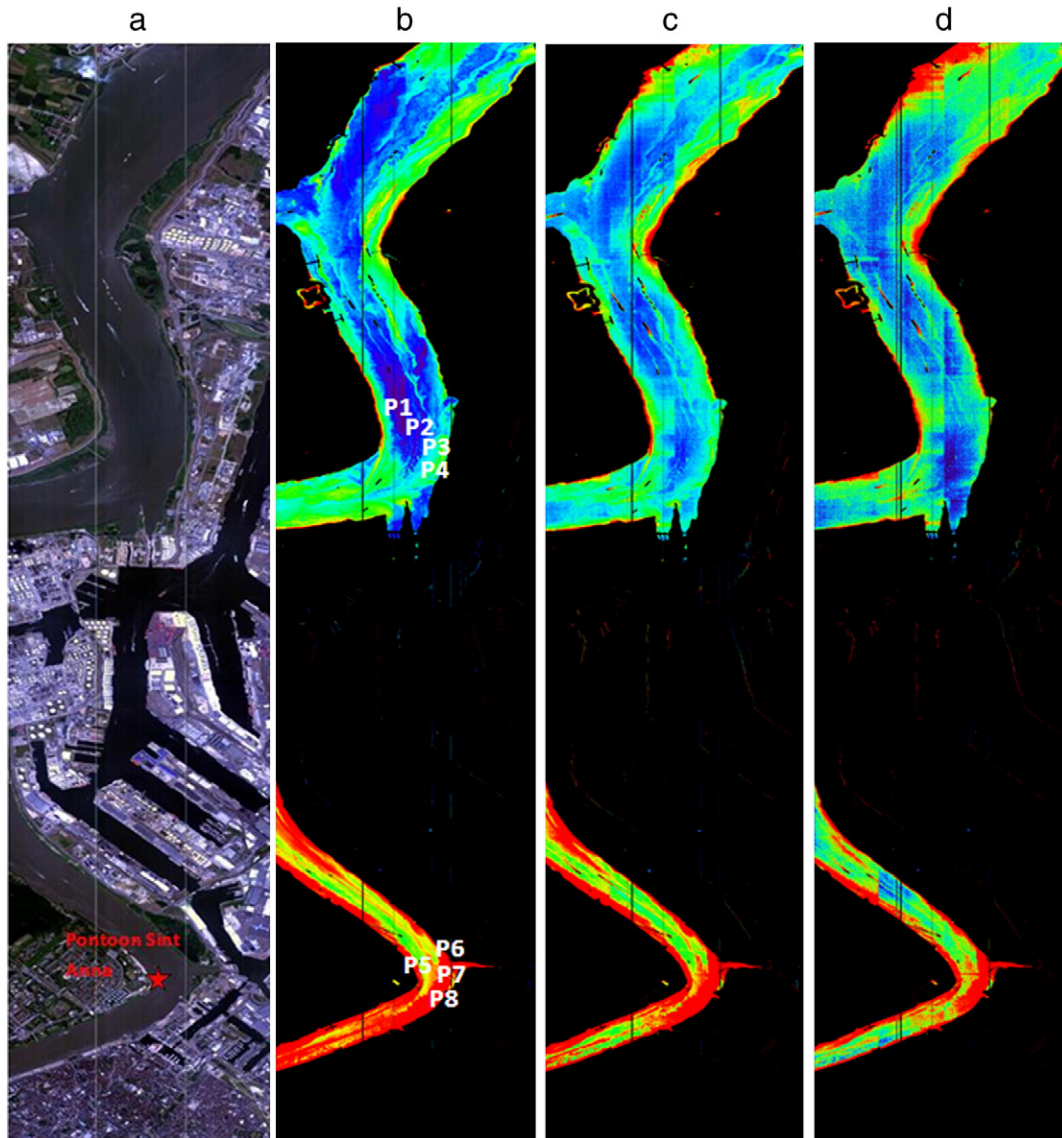**Fig. 14.** Simulated reflectance spectra.

Fig. 15. (a) RBG APEX image of the Scheldt, (b) map of Rw711/Rw597, (c) map of Rw1069, (d) map of Rw1020.

the black pixel assumption can be applied at 1020 nm for a TSM concentration of up to about 35 mg L^{-1}. For the same threshold the black pixel assumption can be applied at 1071 nm for a TSM concentration of up to about 17.5 mg L^{-1}. Using the black pixel assumption in atmospheric correction above these concentration limits can lead to an overestimation of the aerosol contribution and a significant underestimation of the derived reflectance. Hence under these circumstances there is a need for an adjusted atmospheric correction. The quantification of the influence of the misapplication of the black pixel assumption on the reflectance in the SWIR exceeds the scope of the present work, but will be addressed in a future study.

The measurements also show a correlation of the OLCI 1020 nm reflectance with TSM concentration in extremely turbid waters (R = 0.82 and n = 20). These results suggest that spectral bands beyond 1000 nm contain information on the concentrations of optical constituents. The correlation for the spectral band in the center of the absorption peak (1071 nm) was stronger than the correlation for the OLCI band (R = 0.96 versus R = 0.82 and n = 20). This indicates that a proper selection of wavelength for future sensors is essential.

Given the difficulty of achieving longer wavelengths with silicon-based detectors, a band at 1020 nm is recommended as giving already significantly more information that is available from sensors with no SWIR bands (*e.g.* MERIS). Standardization of 1020 nm as a SWIR wavelength for future ocean color sensors gives also advantages for comparison of sensors, whether satellite-based or ground-based, *e.g.* the CIMEL instrument used in the AERONET-OC network (Zibordi et al., 2009), or the MICROPTOPS hand-held sunphotometer.

If additional SWIR bands can be measured then the MODIS 1240 nm, 1640 nm and 2130 nm are obvious candidates. However, the present study suggests that a 1070 nm band would be better than 1020 nm for TSM retrieval because of a stronger marine reflectance signal. Combination of both 1020 nm and 1070 nm bands could allow better discrimination of aerosol and marine reflectance signals

To further investigate SWIR reflectance and test the generality of the current findings, more measurements are needed for a wider range of turbid waters. SWIR reflectance can already be estimated from a number of satellite-borne remote sensors, including MODIS. *In situ* measurements of SWIR reflectance are limited by hardware,
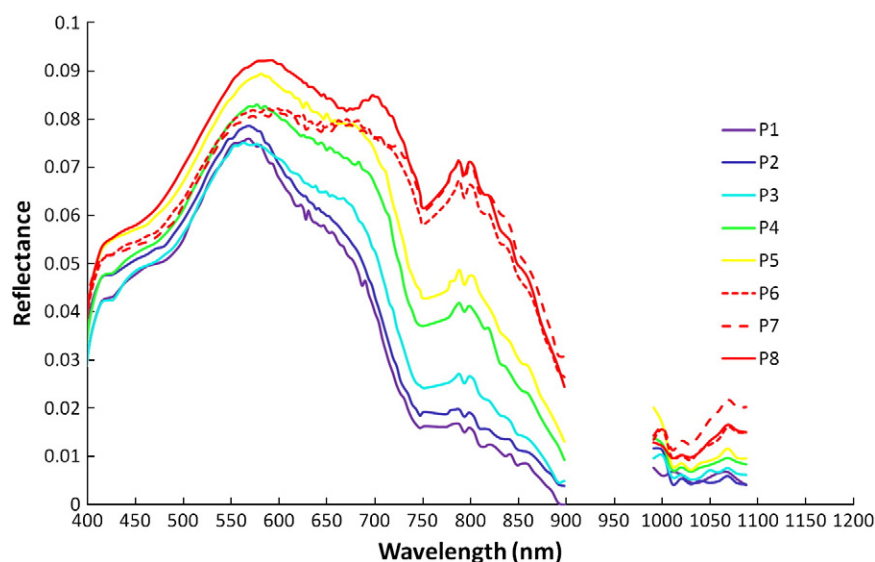
Fig. 16. APEX reflectance spectra at the sites indicated in Fig. 16b.

but new detectors are becoming available to extend current measurements from the near infrared into the SWIR. The measurement of inherent optical properties is a particular gap for the SWIR range. Theory suggests that critical issues will be the possible temperature and salinity dependence of the pure water absorption coefficient as well as the spectral and mass-specific variability of the particulate backscatter coefficient. Instrumentation for measurement of particulate backscatter in the SWIR range, to our knowledge, does not yet exist.

References

Arndt, S., Vanderborght, J. -P., & Regnier, P. (2007). Diatom growth response to physical forcing in a macrotidal estuary: Coupling hydrodynamics, sediment transport, and biogeochemistry. *Journal of Geophysical Research*, *112*.
Baeyens, W., Van Eck, V., Lambert, C., Wollast, R., & Goeyens, L. (1998). General description of the Scheldt estuary. *Hydrobiologia*, *366*, 1–14.
Boardman, J. W. (1998). Post-ATREM polishing of AVIRIS apparent reflectance data using EFFORT: A lesson in accuracy versus precision. *Summaries of the 7th JPL Airborne Earth Science Workshop, vol. 1.* (pp. 53): JPL Pub. 97–21.
Bowers, D. G., Boudjelas, S., & Harker, G. E. L. (1998). The distribution of fine suspended sediments in the Irish Sea and its dependence on tidal stirring. *International Journal of Remote Sensing*, *19*, 2789–2805.
Bricaud, A., & Morel, A. (1986). Light attenuation and scattering by phytoplanktonic cells: A theoretical modeling. *Applied Optics*, *25*(4), 571–580.
Chen, D., Huang, J., & Jackson, T. J. (2005). Vegetation water content estimation for corn and soybeans using spectral indices derived from MODIS near- and short-wave infrared bands. *Remote Sensing of Environment*, *98*(2–3), 225–236.
Chen, Z., Curran, P., & Hansom, J. D. (1992). Derivative reflectance spectroscopy to estimate suspended sediment concentration. *Remote Sensing of Environment*, *40*(1), 67–77.
De Haan, J. F., Hovenier, J. W., Kokke, J. M. M., & Van Stokkom, H. T. C. (1991). Removal of atmospheric influences on satellite-borne imagery: A radiative transfer approach. *Remote Sensing of Environment*, *37*, 1–21.
De Haan, J. F., & Kokke, J. M. M. (1996). Remote sensing algorithm development toolkit I: Operationalization of atmospheric correction methods for tidal and inland waters (Netherlands Remote Sensing Board (BCRS)) publication. *Rijkswaterstaat Survey Dept. Technical Report* 91 pp.
Doxaran, D., Froidefond, J. M., & Castaing, P. (2003). Remote-sensing reflectance of turbid sediment-dominated waters. Reduction of sediment type variations and changing illumination conditions effects by use of reflectance ratios. *Applied Optics*, *42*, 2623–2634.

EN 872 (2005). *Water quality — European reference method for the Determination of suspended solids — Method by filtration through glass fibre filters.* European Committee for Standardization (CEN).
Fettweis, M., Sas, M., & Monbaliu, J. (1998). Seasonal, neap-spring and tidal variations of cohesive sediment concentrations in the Scheldt estuary. *Belgium, Estuarine, Coastal and Shelf Science*, *47*, 21–36.
Gege, P., Fries, J., Haschberger, P., Schötz, P., Schwarzer, H., Strobl, P., et al. (2009). Calibration facility for airborne imaging spectrometers. *ISPRS Journal of Photogrammetry and Remote Sensing*, *64*, 387–397.
Gordon, H. R., & Wang, M. (1994). Retrieval of water-leaving radiance and aerosol optical thickness over the oceans with SeaWiFS: A preliminary algorithm. *Applied Optics*, *33*(3), 443–452.
Hooker, S. B., & Lazin, G. (2000). The SeaBOARR-99 field campaign. *NASA Technical Memorandum 2000–206892, Volume 8.* (pp. 46).
Itten, K. I., Dell'Endice, F., Hueni, A., Kneubühler, M., Schläpfer, D., Odermatt, D., et al. (2008). APEX — The hyperspectral ESA Airborne Prism Experiment. *Sensors*, *8*(10), 6235–6259.
Knaeps, E., Sterckx, S., & Raymaekers, D. (2010). A seasonally robust empirical algorithm to retrieve suspended sediment concentrations in the Scheldt river. *Remote Sensing*, *2*(9), 2040–2059.
Kou, L., Labrie, D., & Chylek, P. (1993). Refractive indices of water and ice in the 0.65–2.5 m spectral range. *Applied Optics*, *32*, 3531–3540.
Lavender, S. J., Pinkerton, M. H., Moore, G. F., Aiken, J., & Blondeau-Patissier, D. (2005). Modification to the atmospheric correction of SeaWiFS ocean color images over turbid waters. *Continental Shelf Research*, *25*, 539–555.
Mobley, C. D. (1999). Estimation of the remote-sensing reflectance from above-surface measurements. *Appied Optics*, *38*, 7442–7455.
Moore, G. F., Aiken, J., & Lavender, S. J. (1999). The atmospheric correction of water colour and the quantitative retrieval of suspended particulate matter in Case II waters: Application to MERIS. *International Journal of Remote Sensing*, *20*(9), 1713–1734.
Morel, A., & Prieur, L. (1977). Analysis of variations in ocean color. *Limnology and Oceanography*, *22*(4), 709–722.
Nechad, B., Ruddick, K. G., & Neukermans, G. (2009). Calibration and validation of a generic multisensor algorithm for mapping of turbidity in coastal waters. *Proceedings of SPIE "Remote Sensing of the Ocean, Sea Ice, and Large Water Regions", Berlin, Germany, 31 August 2009.*
Nechad, B., Ruddick, K. G., & Park, Y. (2010). Calibration and validation of a generic multisensor algorithm for mapping of Total Suspended Matter in turbid waters. *Remote Sensing of Environment*, *114*(4), 854–866.
Pope, R. M., & Fry, E. S. (1997). Absorption spectrum (380–700 nm) of pure water. II. Integrating cavity measurements. *Applied Optics*, *36*, 8710–8723.
Ruddick, K., De Cauwer, V., Park, Y., & Moore, G. (2006). Seaborne measurements of near infrared water-leaving reflectance: The similarity spectrum for turbid waters. *Limnology and Oceanography*, *51*, 1167–1179.
Ruddick, K. G., Ovidio, F., & Rijkeboer, M. (2000). Atmospheric correction of SeaWiFS imagery for turbid coastal and inland waters. *Applied Optics*, *39*, 897–912.
Sgavetti, M., Longhi, I., Meli, S., & Pompilio, L. (2006). Accuracy in mineral identification: Image spectral and spatial resolutions and mineral spectral properties. *Annals of Geophysics*, *49*(1).
Shi, W., & Wang, M. (2009). An assessment of the ocean black pixel assumption for the MODIS SWIR bands. *Remote Sensing of Environment*, *113*, 1587–1597.
Snyder, W. A., Arnone, R. A., Davis, C. O., Goode, W., Gould, R. W., Ladner, S., et al. (2008). Optical scattering and backscattering by organic and inorganic particulates in U.S. Coastal waters. *Applied Optics*, *47*(5), 666–677.

Sterckx, S., Knaeps, E., & Ruddick, K. (2011). Detection and correction of adjacency effects in hyperspectral airborne data of coastal and inland waters: The use of the near infrared similarity spectrum. *International Journal of Remote Sensing*, *32*(21), 6479–6505.

Stumpf, R. P., Arnone, R. A., Gould, R. W., Martinolich, P. M., & Ransibrahmanakul, V. (2003). A partially coupled ocean–atmosphere model for retrieval of water-leaving radiance from SeaWiFS in coastal waters, SeaWiFS Postlaunch Technical Repor Series, Vol. 22, NASA Tech. Memo. 2003–206892, S. B. Hooker and E. R. Firestone, Eds., p51–59, NASA Goddard Space Flight Center, Greenbelt, Maryland.

Tassan, S., & Ferrari, G. M. (1995). An alternative approach to absorption measurements of aquatic particles retained on filters. *Limnology and Oceanography*, *40*, 1358–1368.

Tilstone, G., Moore, G., Sorensen, K., Doerffer, R., Rottgers, R., Ruddick, K. G., et al. (2003). REVAMP regional validation of MERIS chlorophyll products in North Sea coastal waters: Protocols document. *Proceedings of MERIS and AATSR Calibration and Geophysical Validation (MAVT-2003)*. Frascati: European Space Agency Publication WPP-233.

Toole, D. A., Siegel, D. A., Menzies, D. W., Neumann, M. J., & Smith, R. C. (2000). Remote-sensing reflectance determinations in the coastal ocean environment: Impact of instrumental characteristics and environmental variability. *Applied Optics*, *3*(39), 456–469.

Wang, M., & Shi, W. (2007). The NIR-SWIR combined atmospheric correction approach for MODIS ocean color data processing. *Optics Express*, *15*, 15722–15733.

Wetlabs, Inc. (2008). *ECO 3-measurement sensor user's guide.*

Zibordi, G., Holben, B., Slutsker, I., Giles, D., D'Alimonte, D., Mélin, F., et al. (2009). AERONET-OC: A network for the validation of ocean color primary product. *Journal of Atmospheric and Oceanic Technology*, *26*, 1634–1651.